Pergamon

Geochimica et Cosmochimica Acta, Vol. 66, No. 23, pp. 4165–4176, 2002

0016-7037/02 $22.00 + .00

PII S0016-7037(02)00998-5

Solubility of enstatite + forsterite in H_2O at deep crust/upper mantle conditions: 4 to 15 kbar and 700 to 900°C

ROBERT C. NEWTON and CRAIG E. MANNING*

Department of Earth and Space Sciences, University of California at Los Angeles, Los Angeles, CA 90095-1567

(*Received June* 18, 2001; *accepted in revised form June* 3, 2002)

Abstract—Ten reversed brackets of aqueous silica concentration in equilibrium with enstatite ($Mg_2Si_2O_6$) and forsterite (Mg_2SiO_4) were determined at 700 to 900°C and 4.35 to 14 kbar. Silica solubilities were measured by a weight loss-weight gain method and by approaching equilibrium from higher and lower silica concentrations. Both single-crystal and fine-grained synthetic enstatite and forsterite starting material were used, as well as low-Fe natural minerals. Results for all three kinds of starting material were concordant. Silica concentrations buffered by enstatite + forsterite at 10 kbar increase from 0.16 moles/kg H_2O (m) at 700°C to 0.50 m at 900°C, but show only small variation with pressure in the range 7 to 14 kbar. The ratio X_S^Q/X_S^{FE}, where X_S^Q is the mole fraction of aqueous SiO_2 (S) in equilibrium with quartz (Q) from Manning (1994), and X_S^{FE} is the corresponding mole fraction in equilibrium with forsterite (F) and enstatite (E) at the same P and T, from 1 to 15 kbar and 700 to 900°C is described by

$$\frac{X_S^Q}{X_S^{FE}} = 2.61 - 0.000930T + 0.0236P + \frac{290P}{T}$$

where P is in kbar and T in Kelvins. All of our measured silica solubilities are significantly lower than predicted with the conventional assumption of unit activity of silica for concentrations from zero to quartz saturation. Aqueous silica therefore exhibits negative, composition-dependent departures from ideality, in agreement with the deduction of Zhang and Frantz (2000) based on measurements at higher temperatures. Zhang and Frantz (2000) suggested that the formation of solute silica dimers accounts for the lowered activity. The equilibrium constant, K, for the proposed dimer formation reaction, $2H_4SiO_4 = H_6Si_2O_7 + H_2O$, is $K = X_{\text{dimers}}a_{H_2O}/X^2_{\text{monomers}}$, where the activities ($a$) of solute species are equated with their mole fractions, and $a_{H_20} \approx 1$ at the low SiO_2 concentrations considered. Our solubility data at 700°C and 10 kbar give $\log K = 2.2$, which predicts that solute silica in equilibrium with quartz at these conditions is about 40% polymerized, assuming dimers are the only polymer species. This estimate is in good agreement with Raman spectroscopic results of Zotov and Keppler (2002). However, if higher polymers, including rings and chains, are also present, the estimates of K based on either the solubility measurements or the spectroscopic observations would be substantially smaller. Our solubility measurements show that the activity of aqueous silica is substantially less than the molar concentration at deep crust/upper mantle PT conditions.

1. INTRODUCTION

Mass transport by migrating fluids is an important process whose effects in differentiation of the outer earth are increasingly recognized as new quantitative models are applied to the study of fluid-rock interactions. For example, chemical and petrologic studies of metasomatism around some large granite bodies have revealed that integrated fluid fluxes in the metamorphic envelope were much larger than previously suspected (Ferry, 1994). Some well-studied metamorphic terranes, formerly thought to have experienced nearly isochemical metamorphism, may have suffered large net mass changes (e.g., Ague, 1994). Chemical petrology and stable isotope modeling of some high P/T subduction-related metamorphic terranes have shown that huge quantities of aqueous fluids were introduced during the metamorphic alteration (Bebout and Barton, 1989).

Silica is one of the most soluble major rock components at high pressures and temperatures. At conditions of deep crustal metamorphism (700 to 900°C, 5 to 10 kbar), SiO_2 amounts to several weight percent of an aqueous fluid phase in equilibrium with quartz-bearing rocks (Anderson and Burnham, 1965; Manning, 1994). Quartz solubility increases greatly at conditions approaching 1060°C and 9.7 kbar, the upper critical end point in the system SiO_2-H_2O, above which point hydrous SiO_2 melt and SiO_2-rich aqueous fluid are indistinguishable (Kennedy et al., 1962).

A comprehensive dataset of quartz solubility in (initially) pure H_2O exists (Anderson and Burnham, 1965; Manning, 1994) for PT conditions which prevail in the deep crust and upper mantle, but only fragmentary data exist for other important rock-forming minerals, especially in very silica-undersaturated assemblages such as those of ultramafic mantle rocks. Such information can be constructed from the quartz solubility

* Author to whom correspondence should be addressed (manning@ess.ucla.edu).

data and measured thermodynamic properties of very dilute aqueous silica at low pressures and temperatures in conjunction with standard thermodynamic datasets for rock-forming minerals (Holland and Powell, 1998; Berman, 1988). However, extrapolated thermodynamic properties of aqueous silica become increasingly uncertain in the elevated *P* and *T* of deep-seated processes. Activity-concentration relations in the simple system SiO_2-H_2O at these conditions have not been directly measured. Thermodynamic analyses (Walther and Helgeson, 1977; Walther and Orville, 1983) have led to the the assumption that the activity coefficient of total dissolved silica (γ_S) relative to the conventional dilute-solution standard state remains unity for solutions of up to a few mole percent SiO_2. This assumption is widely used in the derivation of thermodynamic data from solubility experiments and the computation of phase equilibria from data sets (e.g., Helgeson et al., 1978; Berman, 1988; Holland and Powell, 1998). For example, the ideal model for aqueous silica appears in calculations of stable mineral assemblages in SiO_2-undersaturated mafic and ultramafic systems in the presence of H_2O at variable activity (Manning, 1995; Newton and Manning, 2000a).

A recent phase-equilibrium study of silica solubility in the quartz-undersaturated region of the system MgO-SiO_2-H_2O at 900 to 1200°C and 10 to 20 kbar (Zhang and Frantz, 2000) throws considerable doubt on the validity of the ideal solution model of aqueous silica at these *PT* conditions. These workers synthesized assemblages of forsterite (Mg_2SiO_4), forsterite + enstatite ($Mg_2Si_2O_6$) or enstatite from oxides in H_2O-dominated bulk compositions of low SiO_2. Vapor-phase compositions in the presence of forsterite+ enstatite were determined from the compositional boundaries of that assemblage projected to the H_2O-SiO_2 subsystem axis, assuming that MgO vapor-phase concentrations are negligible at these conditions. This method was pioneered by Nakamura and Kushiro (1974), who determined enstatite solubility at 15 kbar, at 1280 and 1310°C. Zhang and Frantz (2000) used these points, together with their own data and one measurement at 700°C and 10 kbar on a natural enstatite by Manning and Boettcher (1994) to derive a general formula for enstatite solubility as a function of temperature, believed to be valid at 10 kbar and higher pressures.

The derived solubility of enstatite is much lower than predicted by the standard thermodynamic datasets with $\gamma_S = 1$. To explain the low solubility, γ_S in a fluid in equilibrium with enstatite and forterite at 900°C and 10 kbar could be no higher than 0.5, despite the dilute silica concentration (less than one mole percent). Zhang and Frantz (2000) tentatively ascribed the surprisingly low total dissolved silica ($SiO_{2,aq}$) to dimer formation. This interpretation is supported by recent in-situ Raman spectroscopic observations on quartz-saturated H_2O at conditions up to 900°C and 14 kbar in an externally-heated diamond-anvil apparatus (Zotov and Keppler, 2000). The Raman pattern is dominated by the Si-O stretching frequency of the H_4SiO_4 (orthosilicic acid) molecule. Three new spectral bands which can be attributed to stretching and bending frequencies of additional $H_6Si_2O_7$ dimmers appear at the highest *P* and *T*.

Zotov and Keppler (2002) introduced quantitative estimates of the concentration of silica dimers based on the areas of Raman spectral bands attributed to polymeric silica. They compared the areas of a very broad Raman band centered at 630 cm^{-1}, representing polymerized silica, with the sharp and intense peak at 780 cm^{-1} of the monomeric orthosilicic acid molecule. Absolute silica concentrations in equilibrium with quartz were calibrated on the empirical formula of Fournier and Potter (1982). At the highest *PT* conditions of their study, 900°C and 14.0 ± 2.3 kbar, the silica concentration is near 4 mol percent, with inferred polymeric species accounting for ~75% of the dissolved silica. The diffuseness of the polymeric band compared to the monomeric peak could result in part from the presence of significant amounts of trimeric or higher polymeric species (Zotov and Keppler, 2002).

Although the phase-equilibrium and spectroscopic studies are mutually confirmatory, both studies involve indirect measurements. Zhang and Frantz (2000) utilized projection of phase boundaries, which introduces large uncertainty, and reversibility of the phase assemblages was not determined. The spectroscopic measurements of Zotov and Keppler (2002) were constrained to isochoric *PT* paths, and considerable interpretation is necessary to reduce the Raman measurements to solubility and polymerization values. Thus, more direct solubility measurements are desirable for quantitative evaluation of activity-composition relations for aqueous silica, and application to metasomatic phase relations. The present study was undertaken to measure the concentration of dissolved silica buffered by the reaction:

$$\underset{\text{enstatite}}{Mg_2Si_2O_6} = \underset{\text{forsterite}}{Mg_2SiO_4} = SiO_{2,aq} \quad (1)$$

Accurate and precise determination of the solubility of silica in equilibrium with enstatite and forsterite can be used in combination with quartz solubility measurements (Manning, 1994) to constrain activity-composition models for aqueous silica at high *P* and *T*. Solubility measurements potentially allow quantitative estimates of the speciation of aqueous silica which may be compared with the diamond cell spectroscopic studies. The resulting information allows assessment of the role of polymerization in phase equilibrium and metasomatic mass transfer.

2. EXPERIMENTAL METHODS

Both synthetic, end-member and natural, low-Fe enstatite and forsterite were used as starting materials. Synthetic orthoenstatite grown by Ito (1975) was available in limited amount. The limpid, mostly inclusion-free crystals of 1 to 3 mm length and 1 to 4 mg weight (Fig. 1a), were grown in the orthoenstatite field of stability at one bar by the flux-melt method. Essentially similar forsterite crystals, also grown by Ito, were used as well. In two experiments we used synthetic forsterite grown by H. Takei by the floating-zone method (Takei and Hosoya, 1985). In addition, we hydrothermally synthesized a mixture of fine-grained enstatite and forsterite in about equal mass proportions. Puratronic ultrapure MgO and SiO_2 (quartz) were intimately mixed under distilled H_2O and sealed with 10 wt. % H_2O in Pt containers. Synthesis runs at 900°C and 12 kbar for 24 h yielded a mixture of enstatite, in elongate 10 to 150 μm crystals, and forsterite in equant 2 to 10 μm crystals. Unit-cell constants of enstatite were determined by powder X-ray diffraction in diffractometer scans from 20 to 60° 2θ (Cu, Kα_1) using the forsterite reflections as an internal standard. The enstatite cell constants (a = 18.233(3), b = 8.815(2), c = 5.177(1), in nanometers, with 1σ errors) were identical, within uncertainty, to those of enstatite prepared by a similar method by Aranovich and Newton (1998). The final type of starting material was inclusion-free natural enstatite (En86) from Bamble, Norway, and similar forsterite (Fo90) crystals from San Carlos, Arizona. Elongate chips of the natural materials were

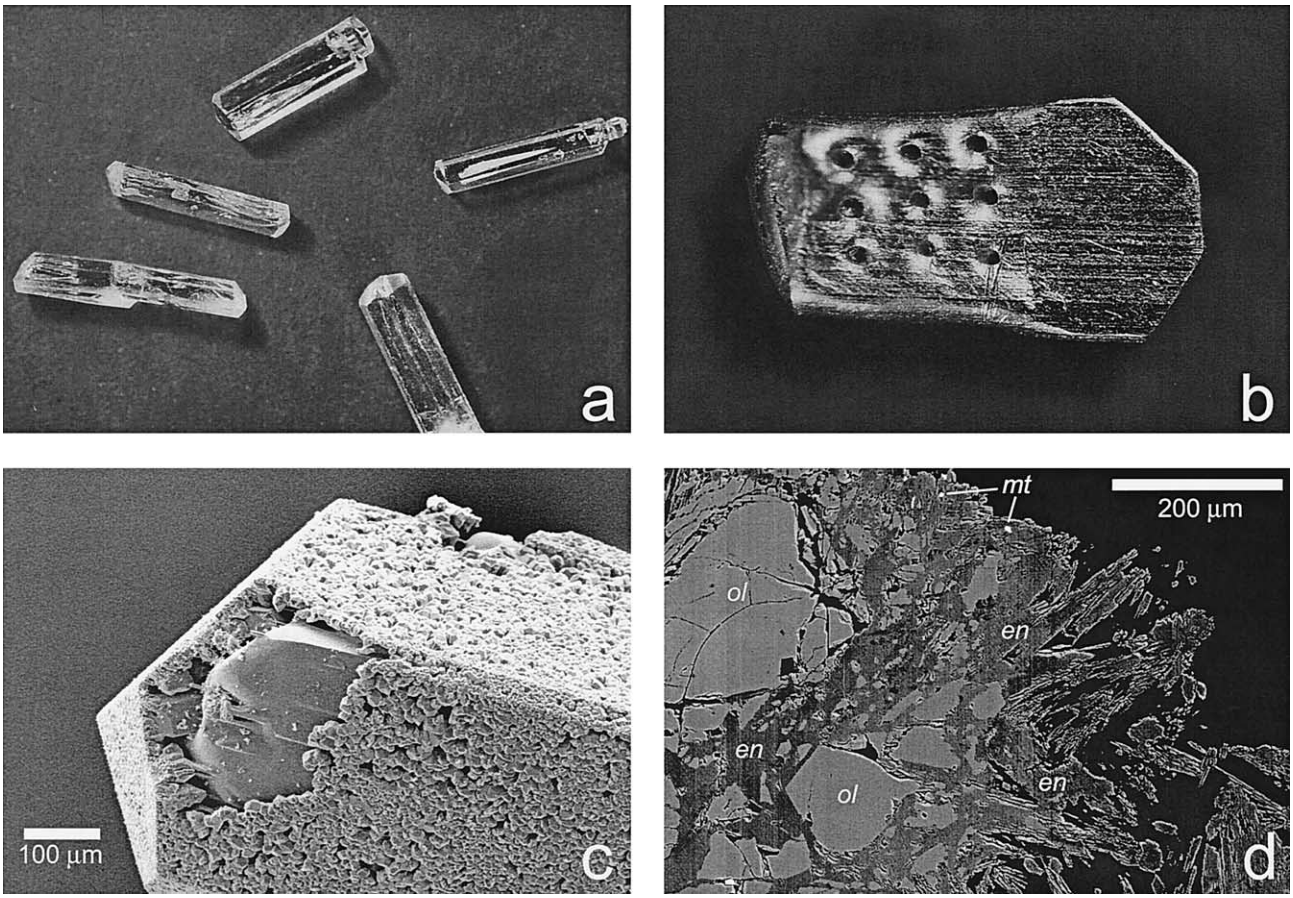

Fig. 1. A. Optical photomicrograph of synthetic, Ito enstatite. Crystals are ~2 mm. B. Optical photomicrograph of preforated inner capsule, after experiment. Capsule length is ~3 mm. C. Secondary electron image of secondary forsterite grains pseudomorphing synthetic enstatite crystal. The forsterite formed by dissolution of silica from enstatite at 10 kbar, 700°C (experiment 2, Table 1). D. Backscattered electron image of enstatite replacing and overgrowing natural forsterite, in an experiment at 10 kbar, 800°C. The original olivine (ol) crystal disaggregated during the experiment; interstices were filled by enstatite (en) and trace magnetite (mt). Euhedral enstatite crystals grew into the fluid at the edges of the olivine + enstatite mass.

ground and polished by rolling on 600-mesh alundum paper to sizes similar to those of the synthetic crystals. Quartz in the reversal experiments on fine-grained synthetic material was 0.4 to 1.2 mg chips of the natural quartz used by Manning (1994).

Experimental assemblies were identical to those used by Newton and Manning (2000b) except for separate encapsulation of the crystalline starting materials, which was necessary to contain granular reaction products. In brief, the 1.91 cm-diameter NaCl piston-cylinder medium with cylindrical graphite heater shell enclosed a welded Pt outer capsule formed from a length of 3 mm diameter tubing with 0.15 mm wall thickness. The outer capsule contained ~25 mg of H_2O and a small inner Pt capsule enclosing the crystalline starting material, either enstatite or forsterite. The inner capsule, ~3 mm in length and weighing ~65 mg, was punctured with numerous small holes to allow access of the external H_2O (Fig. 1b). This method was used in the quartz solubility studies of Anderson and Burnham (1965) and Manning (1994).

All experiments were made by the piston-out method of pressing and heating. Assemblies were pressed cold to a pressure 3 kbar below the final desired pressure and heated to the final temperature. Thermal expansion of the NaCl-dominated assemblies brought the pressure to the desired nominal value. At temperatures above 600°C some bleeding of the gauge pressure was required to prevent overshoot. No pressure correction is necessary with the piston-out method above 5 kbar; a +350 bar correction was applied at 4.35 kbar (Newton and Manning, 2000b). Pressures are accurate to ±300 bars. Temperatures were measured and controlled automatically using calibrated matched pairs of W3%Re vs. W25%Re thermocouples. A thermocouple tip was in contact with the sample capsule, though protected by a film of Al_2O_3 cement. Temperatures are considered accurate to ±3°C.

The silica content of the fluid was determined by weight loss or gain of the inner capsule. All weight change can be ascribed to change in Si content of the charge because Mg solubility over the conditions of our experiments has been shown to be negligible compared to Si solubility (Zhang and Frantz, 2000). Similarly, the maximum OH^- contents of enstatite and forsterite grown hydrothermally in the present *PT* range are smaller than could be observable by our weight loss technique (Bell and Rossman, 1992).

Silica solubility at a given *P* and *T* was established by approaching equilibrium solubility from higher and lower initial concentrations. Weight loss of a quenched inner capsule loaded with a single crystal of enstatite determined the silica content of the fluid approached from low, enstatite-undersaturated Si concentration as reaction (1) moved to the right. By contrast, weight gain of an inner capsule containing enstatite and forsterite, sealed within an outer capsule containing H_2O and a small natural quartz crystal established final Si solubility as approached from higher initial Si concentration as Reaction (1) was driven to the left. Approach from higher solubility requires that (1) the mass of quartz was sufficient to react only a portion of the forsterite in the inner capsule to enstatite; (2) the quartz crystal dissolved completely; and (3) the quartz crystal dissolved rapidly relative to enstatite-forsterite-fluid equlibration (see below). Addition of a small quartz crystal to provide

an initial fluid silica content in both forward and reversal experiments with the fine-grained synthetic enstatite-forsterite mix improved the tightness of solubility brackets.

Errors in solubility determination result from weighing uncertainties. Enstatite, forsterite and quartz starting materials and the inner Pt capsules before and after the runs were weighed on a Mettler M3 microbalance. Water contents of the charges were determined by weighing upon loading, as well as after experiments by puncturing and drying of the outer capsules. The water contents so determined agreed within 0.6%. The drying loss measurements were considered more reliable and were therefore used to calculate solubility. Repeated test weighings over the course of this study yielded normally distributed errors with $1\sigma = 0.002$ mg. Weighing errors were propagated to solubility determinations by assigning this value to each weighing step used in the calculations.

3. RESULTS OF EXPERIMENTS

Weight-change data and calculated silica solubilities are given in Table 1. As expected, experiments with enstatite starting material showed substantial weight losses of the inner capsules, presumably resulting from leaching of silica, leaving a residue of forsterite. Consistent with this interpretation, the runs with forsterite and quartz showed weight gains of the inner capsules, some of the forsterite having been converted to enstatite. These interpretations were verified by scanning electron microscopy and X-ray diffraction of the quenched charges from the inner capsules. Figure 1c is a scanning electron microscope image of the charge of experiment 2 at 700°C, 10 kbar, which used synthetic single-crystal enstatite (Table 1). The original enstatite grain is coated with well-formed granular forsterite. The geometry of the original enstatite is preserved pseudomorphically. Figure 1d shows a portion of an experiment on natural forsterite and quartz (800°C, 10 kbar). The original olivine crystal has been disaggregated into subangular grains and is surrounded by an enstatite matrix with trace magnetite. Most of the new enstatite was in the form of euhedral, prismatic crystals grown at the margins of the two-phase mass. Enstatite in the interstices between olivine grains contains 4.0 to 6.0 wt % FeO, whereas prismatic enstatite at the margins has only 1 to 2 wt % FeO. Olivines retain their original FeO concentrations (11 wt %). The presence of enstatite confirms that the weight gains in the reversal runs were the result of enstatite growth.

Experiments with forsterite single crystals + quartz produced talc instead of enstatite at 600 and 700°C. At 600°C and 10 kbar, talc and forsterite are stable relative to enstatite and H_2O fluid (Holland and Powell, 1998). At 700°C and 10 kbar, however, enstatite + H_2O are stable by 10 to 20°C relative to forsterite + talc. We interpret the formation of talc in forsterite + quartz experiments at this pressure and temperature as metastable growth from forsterite and the SiO_2-oversaturated aqueous fluid. Experiments with the fine-grained forsterite-enstatite mix + quartz did not produce talc at 700°C. Talc was not found at $\geq$800°C.

An experiment was made to verify that quartz dissolution is much faster than enstatite-forsterite-fluid equilibration. A 1-mg quartz crystal dissolved completely in 32 mg of H_2O in two hours at 700°C and 10 kbar. This demonstrates that the effective initial concentrations of $SiO_{2,aq}$ in the reversal experiments starting with forsterite + quartz + H_2O were higher than the final, equilibrium value.

Four control experiments were made to check for spurious solubility contributions from flux inclusions in synthetic single-crystal starting materials or weight changes of the Pt of the inner capsules (Table 2). Two experiments with only the Ito forsterite (no quartz) yielded losses of 0.011 and 0.009 mg, compared with the maximum expected weight loss of 0.003 mg at the experimental conditions, based on calculations of forsterite solubility assuming $\gamma_s = 1$ (Newton and Manning, 2000a). An experiment on an empty Pt capsule at 700°C and 10 kbar showed a weight loss of 0.003 mg; a simlar experiment at 800°C, 10 kbar, showed no detectable weight loss. Taken together, the empty-capsule experiments indicate no detectable Pt weight loss, given weighing error of $1\sigma = 0.002$ mg. These data indicate that the Ito forsterite gives a spurious weight loss of 0.007 mg for a 1 to 2 mg crystal, possibly from the presence of minute flux inclusions in the crystals. Accordingly, a small correction of 0.007 mg was made in Table 1 for the experiments on synthetic single crystals.

Experiments with natural enstatite and forsterite at 700°C yielded shiny black crystals on the insides of the inner capsules. X-ray diffraction showed them to be magnetite. At 600°C the charges had a rosy cast, suggesting the presence of hematite as well. Magnetite and/or hematite presumably resulted from a disproportionation reaction with concomitant reduction of some FeO to Fe metal dissolved in the Pt capsule. At 800 and 850°C, only trace magnetite was observed in experiments on natural materials (Fig. 1d), and the charges were colorless. Newly grown minerals (enstatite or forsterite) at 800°C were low in Fe, whereas residual unreacted minerals retained their original compositions. This indicates that most of the original Fe alloyed with the Pt capsules during the dissolution process. The weight changes for natural enstatite and forsterite are corrected by assuming that all of the Fe from recrystallized materials in the 800 and 850°C runs was retained in the inner capsule, but that the O_2 escaped. The presence of magnetite in the 700°C charges indicates that no correction should be made at that temperature. Under these assumptions, the small weight-loss correction for Fe in Table 1 is proportional to the reaction progress, as indicated by the total weight change. The corrections lower the calculated SiO_2 molalities slightly.

Figure 2 shows the 10-kbar solubility determinations on all starting materials as a function of experiment duration. Experiments approaching final solubility from higher and lower initial concentrations respectively define upper and lower bounds on the equilibrium solubility at a given temperature. The solubilities determined from initially undersaturated and oversaturated conditions approach each other closely for experiments longer than 100 h at $>$700°C. The natural minerals yield brackets which are consistent with results from synthetic materials, when the Fe corrections are made; nevertheless, brackets taken to be definitive in this study are based on experiments using synthetic materials.

The very small pressure effect of enstatite solubility above 10 kbar, as noted by Zhang and Frantz (2000) and confirmed by our data, allows a direct comparison among all available studies at 10 to 15 kbar (Fig. 3). Our reversed bracket at 900°C and 10 kbar falls just outside the uncertainty interval of Zhang and Frantz (2000), and the trend departs from theirs to lower temperatures. Our four points at 10 kbar are described by the linear relation:

Table 1. Experimental data on the solubility of forsterite + enstatite in H_2O.

P (kbar)	T (°C)	Expt. no.	Starting material	Time (hr)	Wt qz in (mg)	Wt H_2O (mg)	Wt E/F in (mg)	Wt inner capsule in (mg)	Wt inner capsule out (mg)	Nominal m_{SiO_2} (mol/kg)	Adjusted m_{SiO_2} †	10^3 X_{SiO_2}
10	600	25	FQ/N	84	0.304	20.997	3.610	55.399	55.617*	0.068(3)		1.23(5)
10	600	23	E/N	94		10.438	1.558	55.819	55.777*	0.067(5)		1.21(8)
4.35	700	40	E/S1	63		24.599	1.880	64.459	64.289	0.115(2)	0.112(2)	2.02(3)
4.35	700	39	FQ/S2	89	0.357	25.097	1.185	58.940	59.057*	0.159(2)		2.86(4)
7	700	31	E/S1	93		25.291	2.017	58.019	57.801	0.144(2)	0.141(3)	2.53(3)
7	700	30	FQ/S1	95	0.466	23.020	1.599	53.920	54.126	0.188(3)	0.185(2)	3.33(4)
10	700	15	FQ/S1	23	0.483	21.270	2.226	55.537	55.693*	0.256(3)	0.253(3)	4.54(5)
10	700	2	E/S1	46		21.946	1.612	79.953	79.755	0.150(2)	0.147(2)	2.65(4)
10	700	16	E/SI	62		22.746	1.722	55.793	55.593	0.146(2)	0.144(2)	2.58(4)
10	700	24	E/N	67		25.356	2.181	56.283	56.043	0.158(2)		2.83(3)
10	700	37	FQ/S2	67	0.288	25.489	1.660	56.060	56.055*	0.185(2)		3.32(4)
10	700	19	FQ/S1	85	0.395	22.154	1.636	57.315	57.492*	0.164(3)	0.161(3)	2.89(5)
10	700	3	E/S1	92		16.503	0.998	68.329	68.174	0.156(3)	0.152(3)	2.74(5)
10	700	13	FQ/S1	93	0.335	21.119	1.654	49.917	50.041*	0.166(3)	0.163(3)	2.93(5)
10	700	12	FQ/N	94	0.457	22.358	2.078	50.196	50.396*	0.191(3)	0.189(3)	3.44(5)
10	700	55	EFQ/S3/s	114	0.413	32.454	2.748	69.478	69.574	0.163(2)		2.92(3)
13	700	32	FQ/S1	70	0.529	25.989	1.331	56.703	56.947*	0.183(2)	0.180(2)	3.23(4)
13	700	33	E/S1	91		22.016	0.973	63.633	63.433	0.151(2)	0.148(2)	2.66(4)
7	800	50	EFQ/S3/u	90	0.361	32.430	4.145	71.545	71.414	0.253(2)		4.53(3)
7	800	51	EFQ/S3/s	94	0.630	29.531	1.770	68.891	68.999	0.294(2)		5.28(4)
10	800	7	FQ/S1	22	0.591	20.650	1.583	69.191	69.313	0.378(3)	0.375(3)	6.71(5)
10	800	44	EFQ/S3/u	43		21.632	3.176	82.172	81.906	0.205(2)		3.68(4)
10	800	21	FQ/S1	57	0.491	21.000	1.598	57.343	57.417	0.331(3)	0.328(3)	5.87(5)
10	800	4	E/N	64		17.795	3.826	71.630	71.305	0.304(3)	0.262(2)	4.70(4)
10	800	10	E/N	66		21.622	1.629	53.007	52.621	0.297(2)	0.256(2)	4.60(3)
10	800	6	E/S1	69		14.713	1.807			**0.261(3)**	**0.257(3)**	**4.61(6)**
10	800	9	E/S1	92		20.818	2.112	49.151	48.805	0.277(2)	0.274(2)	4.90(4)
10	800	8	FQ/S1	95	0.482	19.983	1.101	53.220	53.300	0.335(3)	0.332(3)	5.94(5)
10	800	11	FQ/N	95	0.459	20.783	2.019	59.604	59.675	0.311(3)	0.304(3)	5.45(5)
10	800	45	EFQ/S3/u	116	0.393	29.649	3.322	66.752	66.613	0.299(2)		5.35(3)
10	800	46	EFQ/S3/s	117	0.645	31.175	4.050	71.455	71.550	0.294(2)		5.27(3)
12	800	61	EFQ/S3/s	98	0.681	32.894	1.730	60.191	60.309	0.285(2)		5.11(3)
12	800	60	EFQ/S3/u	111	0.430	33.093	1.974	69.388	69.288	0.267(2)		4.78(3)
10	850	27	FQ/N	45	0.820	25.063	3.257	56.799	56.964	0.435(2)	0.422(2)	7.55(4)
10	850	26	E/N	61		20.095	2.745	55.259	54.747	0.424(2)	0.366(2)	6.55(4)
10	850	28	FQ/S1	65	0.763	25.356	1.732	55.083	55.244	0.395(2)	0.393(2)	7.03(4)
10	850	29	E/S1	72		25.688	2.776	59.707	59.144	0.365(2)	0.362(2)	6.49(3)
10	850	49	EFQ/S3/s	94	0.847	30.407	3.747	74.348	74.490	0.386(2)		6.91(3)
10	850	48	EFQ/S3/u	96	0.471	30.505	2.905	77.780	77.574	0.370(2)		6.61(3)
10	900	53	EFQ/S3/u	44	0.658	31.160	3.256	71.511	71.271	0.480(2)		8.57(3)
10	900	54	EFQ/S3/s	45	1.092	31.743	3.977	75.044	75.155	0.515(2)		9.19(3)
14	900	56	EFQ/S3/s	43	1.152	32.364	2.912	68.467	68.594	0.527(2)		9.41(3)
14	900	57	EFQ/S3/u	44	0.780	31.785	4.716	70.797	70.609	0.507(2)		9.05(3)

Data in bold determined by weighing crystalline charge after experiment (1.576 mg) rather than inner capsule. Parenthetical numbers are propagated 1σ weighing uncertainties in last significant figure. Abbreviations: E, enstatite; F, forsterite; Q, quartz; N, natural minerals; S1, synthetic enstatite or forsterite from Ito (1975); S2, synthetic forsterite from Takei (Takei and Hosoya, 1985); S3, synthetic enstatite and forsterite grown hydrothermally (this study); s, equilibrium approached from supersaturation; u, equilibrium approached from undersaturation.

* Talc present in inner capsule.

† Adjustments to SiO_2 concentration for minor flux inclusions in Ito enstatite and forsterite (S1 experiments), and O loss at T ≥ 800°C in N experiments yielded corrected inner capsule weight change (Δ', mg) from nominal inner capsule weight change (Δ, mg) as follows (see text): E/S1, $\Delta' = \Delta - 0.004$; F/S1, $\Delta' = \Delta + 0.004$; E/N at ≥800°C, $\Delta' = \Delta - 0.138\Delta$; Fo/N at ≥800°C, $\Delta' = \Delta + 0.120\Delta$.

Table 2. Results of blank experiments.

P (kbar)	*T* (°C)	Expt. no.	Starting material	Time (hr)	Wt H_2O (mg)	Wt fo in (mg)	Wt inner capsule in (mg)	Wt inner capsule out (mg)	Wt change (mg)
10	700	18	F/S1	70	22.371	1.273	53.892	53.883	−0.009
10	700	20	F/S1	62	21.962	1.173	56.772	56.761	−0.011
10	700	34	—	70	25.701	—	55.887	55.884	−0.003
10	800	59	—	23	32.437	—	64.713	64.713	0.000

Abbreviations as in Table 1.

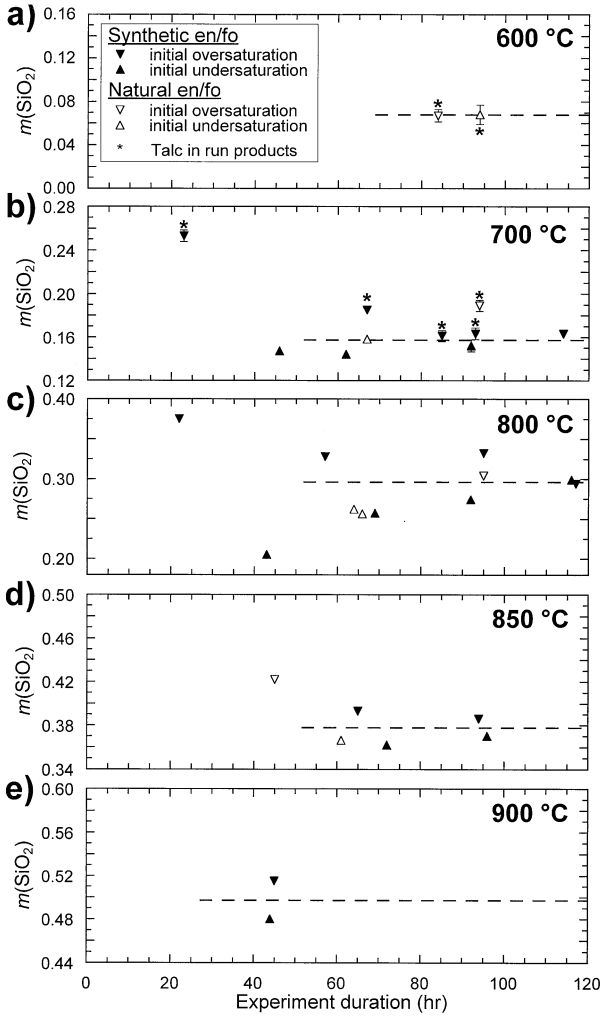

Fig. 2. Molality of silica at 10 kbar vs. experiment duration at 600 (A), 700 (B), 800 (C), 850 (D), and 900°C (E). Upward pointing triangles are experiments approached final Si solubility from low concentration; experiments designated by downward pointing triangles approached final solubility from higher Si concentration. 2σ errors are shown where larger than symbol size. Asterisks denote experiments in which talc was present in run products (see text). Dashed lines are midpoints between maximum and minimum solubility values defined by the most restrictive bracketing experiments involving synthetic starting materials (see text). Abbreviations: En, enstatite; Fo, forsterite.

$$\log m_{SiO_{2,aq}} = 2.006 - 2785/T \quad (2)$$

(T in Kelvins) with a correlation coefficient of −0.9995. Our trend converges on the Zhang and Frantz (2000) trend near 1000°C. Because of the great increase of silica solubility as the upper critical end point in the system SiO_2-H_2O is approached, it is likely that the enstatite solubility curve does indeed swerve to higher concentrations at 10 kbar and temperatures above 1000°C, as depicted by Zhang and Frantz (2000). Our data should give a more accurate account of enstatite solubility in the range below 900°C than the previous estimates for the reasons that our measurements are more direct and of higher precision than those of previous workers, they are reversed determinations, and we have shown concordance of results of three different kinds of starting materials.

A possible explanation for the discrepancy between our data at 900°C and 10 kbar and those of Zhang and Frantz (2000) at the same conditions is that they quenched their experiments

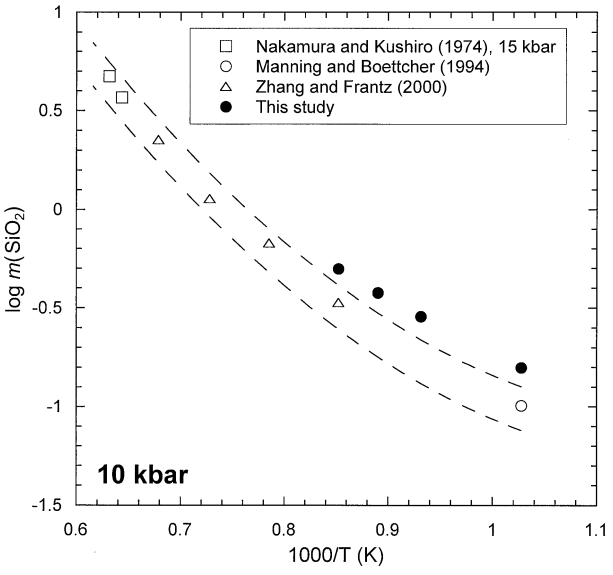

Fig. 3. Comparison of experimental results on m_{SiO_2} in equilibrium with forsterite and enstatite. All experimental results are at 10 kbar, except Nakamura and Kushiro, 1974, which are at 15 kbar. The dashed lines indicate the estimated uncertainty of the Zhang and Frantz (2000) quadratic formula summarizing their data, together with the two points of Nakamura and Kushiro (1974) at 15 kbar and the point of Manning and Boettcher (1994). Our higher solubilities are believed to be more accurate and precise because of improved constraints on equilibrium and greater sensitivity of the weight-loss technique.

Table 3. R_γ, activity coefficients of aqueous silica, and log$K$ at selected experimental conditions.

T (°C)	P (kbar)	$-\Delta G^\circ_{QFE}$ (kJ/mol)	$10^3\ X_S^{FE}$	$10^3\ X_S^{Q}$	R_γ	Dimer model γ_S^{FE}	Dimer model γ_S^{Q}	Dimer model logK_{dm}	All-polymer model γ_S^{FE}	All-polymer model γ_S^{Q}	All-polymer model logK_{ap}
700	1	4.54	0.48(02)	0.99(02)	1.18(06)	0.77(08)	0.65(10)	2.62(27)	0.82(4)	0.70(3)	2.38(04)
700	4.35	6.06	2.44(42)	7.56(36)	1.47(17)	0.58(15)	0.39(15)	2.42(46)	0.75(5)	0.51(7)	1.88(18)
700	7	7.22	2.93(39)	10.73(36)	1.50(13)	0.65(09)	0.44(10)	2.14(27)	0.79(3)	0.52(9)	1.69(18)
700	10	8.47	2.83(10)	13.45(36)	1.67(06)	0.64(03)	0.38(03)	2.20(08)	0.79(1)	0.48(7)	1.69(13)
700	13	9.69	2.95(29)	15.68(36)	1.63(10)	0.72(04)	0.45(05)	1.95(15)	0.83(2)	0.51(2)	1.55(08)
800	7	6.98	4.90(37)	18.03(36)	1.68(08)	0.42(07)	0.25(05)	2.51(21)	0.70(2)	0.42(4)	1.67(06)
800	10	8.31	5.09(18)	23.33(36)	1.81(05)	0.48(03)	0.26(02)	2.36(09)	0.74(1)	0.41(3)	1.58(03)
800	12	9.17	4.95(16)	26.31(36)	1.90(04)	0.50(02)	0.26(02)	2.31(07)	0.75(1)	0.40(1)	1.55(02)
850	10	8.22	6.76(14)	29.73(36)	1.82(03)	0.41(02)	0.23(02)	2.40(07)	0.71(1)	0.39(1)	1.51(02)
900	10	8.12	8.88(31)	37.24(36)	1.83(04)	0.37(03)	0.20(02)	2.43(10)	0.69(1)	0.38(1)	1.43(02)
900	14	9.88	9.23(18)	47.20(36)	1.86(02)	0.51(01)	0.28(01)	2.01(04)	0.75(1)	0.41(1)	1.28(01)

Abbreviations as in Table 1. ΔG°_{QFE} from Holland and Powell (1998, uncertainties ignored). X_S^{FE} values at >1 kbar are midpoints between maximum and minimum solubilities from this study (Table 1), with range given in parentheses. X_S^{FE} at 700°C, 1 kbar from Hemley et al. (1977); uncertainty is 5%. Parenthetical entries after X_S^Q, R_γ, γ_S^{FE}, γ_S^Q and log$K$ are 1σ errors in last digit(s). X_S^Q from Manning (1994; $1\sigma = 0.36 \times 10^{-3}$ except at 1 kbar, where 1σ assumed to be 2.5%). 1σ errors in R_γ, γ_S^{FE}, γ_S^Q and log$K$ calculated by Monte Carlo simulation (5,000 trials) assuming equal probability of any X_S^{FE} value between experimental bracket limits, and normal distribution of errors in X_S^Q.

through the equilibrium field of enstatite (decreasing temperature at nearly constant pressure). Schreyer and Yoder (1964) noted that enstatite can form rapidly in hydrothermal quenching procedures, with possible misinterpretation of phase equilibrium boundaries. Since the projection method of Zhang and Frantz (2000) was based on the presence or absence of enstatite in quenched charges as determined microscopically, it is possible that quench-formed enstatite could have biased their phase boundaries towards lower values of $m_{SiO_{2,aq}}$. The approximately five days' duration necessary to obtain a tightly reversed determination of enstatite solubility at 800°C and 10 kbar suggests that the one-day experiment of Manning and Boettcher (1994) at 700°C and 10 kbar was too short to approach equilibrium solubility closely.

4. DISCUSSION

The present data may be combined with the solubility data of Manning (1994) for the reaction

$$\underset{\text{quartz}}{SiO_2} = SiO_{2,aq} \tag{3}$$

to provide some general information on the solution behavior of solute silica as a function of P, T and silica concentration. Expressions for the equilibrium constants of equilibria (1) and (3) can be combined to give:

$$\ln R_\gamma \equiv \ln \frac{\gamma_S^{FE}}{\gamma_S^{Q}} = \frac{\Delta G^\circ_{QFE}}{RT} + \ln \frac{X_S^{Q}}{X_S^{FE}} \tag{4}$$

where γ_S^{FE} denotes the activity coefficient of $SiO_{2,aq}$ at constant P and T at X_S^{FE}, the concentration of $SiO_{2,aq}$ in equilibrium with enstatite and forsterite, γ_S^Q and X_S^Q are the corresponding quantities at quartz saturation, and ΔG°_{QFE} is the standard Gibbs free energy change of the reaction of quartz and forsterite to enstatite. The standard state of solute silica is taken for convenience to be unit mole fraction of the hypothetical solution of pure silica monomers, but the ratio γ_S^{FE}/γ_S^Q (R_γ) is virtually the same for a molality standard state at the low concentrations considered here. Eqn. 4 shows that when the experimental data of this study are combined with data on quartz solubility, the two datasets constrain R_γ for the enstatite + forsterite and quartz silica buffers. We derived an empirical relation for the variation X_S^Q/X_S^{FE} with P and T, and used this with Eqn. 4 to evaluate silica solution behavior.

4.1. X_S^Q/X_S^{FE} as a Function of P and T

The quantity X_S^Q/X_S^{FE} proves to vary linearly with pressure at constant temperature, and the temperature dependence is quite small in the range 700 to 900°C. As pressure decreases, R_γ must approach unity. Therefore,

$$\lim_{P\to 0} \frac{X_S^Q}{X_S^{FE}} = \exp\left(\frac{-\Delta G^\circ_{QFE}}{RT}\right) \tag{5}$$

The values of ΔG°_{QFE} at $P = 0$ (Holland and Powell, 1998) were combined with high-PT X_S^Q/X_S^{FE} from our experiments at ≥700°C and Manning (1994) to derive the relation

$$\frac{X_S^Q}{X_S^{FE}} = 2.61 - 0.000930T + 0.0236P + \frac{290P}{T} \tag{6}$$

with T in Kelvins and P in kbar. Experimental conditions and data used to derive Eqn. 6 are given in Table 3. Experiments at 600°C, 10 kbar, were omitted because of talc in all run products. The fit was optimized by assuming uniform probability of calculated X_S^Q/X_S^{FE} within the limits of experimental brackets while ignoring uncertainty in quartz solubility. Extrapolation of Eqn. 6 should be limited to the range in which $(\partial X_S^Q/X_S^{FE})/(\partial P)_T$ is approximately linear in $1/T$ (conservatively, 600 to 1000°C).

Solubility isotherms of enstatite + forsterite constrained by Eqn. 6 and the quartz solubility equation of Manning (1994) are shown in Figure 4. SiO_2 concentration in equilibrium with forsterite and enstatite is nearly independent of pressure above 7 to 8 kbar, as stated by Zhang and Frantz (2000). Various kinds of modeling with the Manning (1994) and Holland and Powell (1998) inputs persistently yielded slight solubility maxima near 10 to 12 kbar. Our experimental brackets are not precise enough to confirm this trend. The curves plunge to very

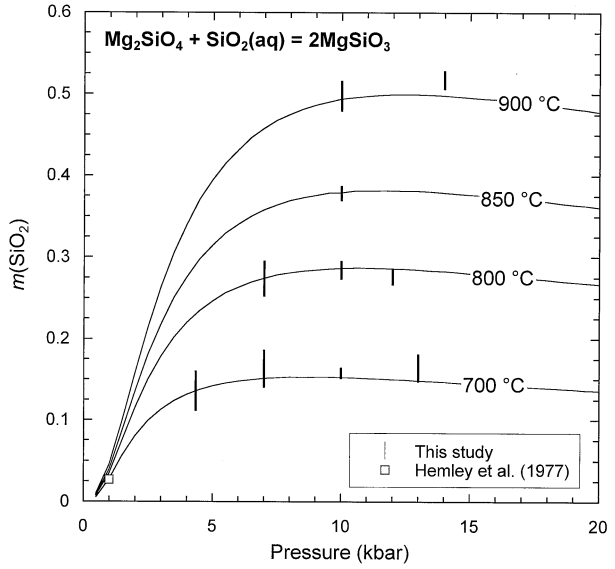

Fig. 4. Calculated m_{SiO_2} isotherms in equilibrium with forsterite + enstatite based on Eqn. 6, compared to experimental results of this study. Vertical lines represent range between minimum and maximum solubility constraints; there is uniform probability of true solubility within this range. Forsterite + enstatite + H_2O are metastable at ~2 to 5 kbar at 700°C.

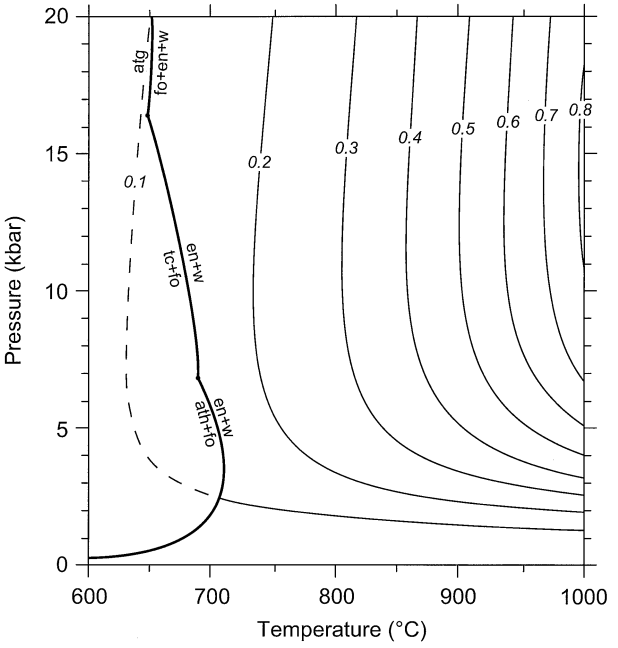

Fig. 5. *PT* projection showing m_{SiO_2} isopleths in the forsterite-enstatite-H_2O stability field, calculated using Eqn. 6 and the data of Holland and Powell (1998). Dashed line indicates metastability of the assemblage. Bold curves denote equilibria defining the low-*T* stability limit of the forsterite-enstatite-H_2O assemblage; small filled circles are invariant points (other equilibria omitted). Abbreviations: atg, antigorite; ath, anthophyllite; en, enstatite; fo, forsterite; tc, talc; w, water.

small silica molality below 5 kbar, following the trend for quartz solubility. Although our results do not constrain X_S^Q/X_S^{FE} in the low-pressure range, Eqn. 5 imposes stringent control on the curves. Our calculated solubility at 700°C and 1 kbar (0.027 *m*) is the same as that measured by Hemley et al. (1977).

Figure 5 shows contours of SiO_2 molality in aqueous solutions in equilibrium with forsterite and enstatite (Eqn. 6). Within the forsterite-enstatite-H_2O stability region, solubility can be seen to be more strongly dependent on *P* than *T* at <3 kbar; the reverse is the case at higher *P*.

4.2. Constraints on Activity-Concentration Relations

Our data cannot define uniquely the activity-concentration relations of solute silica; however, they do constrain the possible solution behavior. Eqn. 4 was used to evaluate the magnitude of deviations from ideality which are required by the experimental data. Values of R_γ from our experiments are given in Table 3. If activity coefficients are unity, which is the assumption usually made in studies of the thermodynamic properties of aqueous silica, or if activity coefficients are constants independent of concentration (that is, if they obey Henry's Law over the observed concentration range), then R_γ would be unity, and the equality in Eqn. 5 would hold to $P > 0$. If activity coefficients are not equal, the right side of Eqn. 4 quantifies the departure from ideality. Values of R_γ are significantly greater than unity at all conditions investigated, consistent with negative departures from ideality. The differences between ΔG°_{QFE} and $RT\ln(X_S^Q/X_S^{FE})$ are 3.2 to 5.6 kJ.

The pronounced non-ideality of solute silica even at quite low concentrations is evident in Figure 6. Measured solubilities are substantially smaller than calculated from the standard datasets using the assumption of unit activity of $SiO_{2,aq}$ at pressures above 1 to 2 kbar, consistent with the findings of Zhang and Frantz (2000) at higher temperatures. At 700°C and 10 kbar, the predicted SiO_2 molality is 0.266, compared with our measured value of 0.158 ± 0.006. At 800°C and 10 kbar, the ideal solution prediction is 0.523, compared with our measured value of 0.284 ± 0.010. At 900°C, the discrepancy between our measurement and the ideal solution prediction amounts to a factor of two.

4.3. Solute Speciation

If the dominant form of aqueous silica at high *T* and *P* and very low concentrations is neutral monomers, then negative departures from ideal-solution behavior at higher concentrations undoubtedly arise from progressive polymerization, as stated by Zhang and Frantz (2000). According to Zotov and Keppler (2000, 2002), a dimer-forming reaction would also be a dehydration reaction:

$$\underset{\text{monomer}}{2H_4SiO_4} = \underset{\text{dimer}}{H_6Si_2O_7} + H_2O \qquad (7)$$

for which

$$K_{dm} = \frac{a_2 a_{H_2O}}{a_1^2} \qquad (8)$$

where the subscript *dm* denotes the dimer-forming reaction. Following Zotov and Keppler (2002), the activities, *a*, of monomers (1) and dimers (2) can, to a first approximation, be equated to their mole fractions. Also, the solutions are suffi-

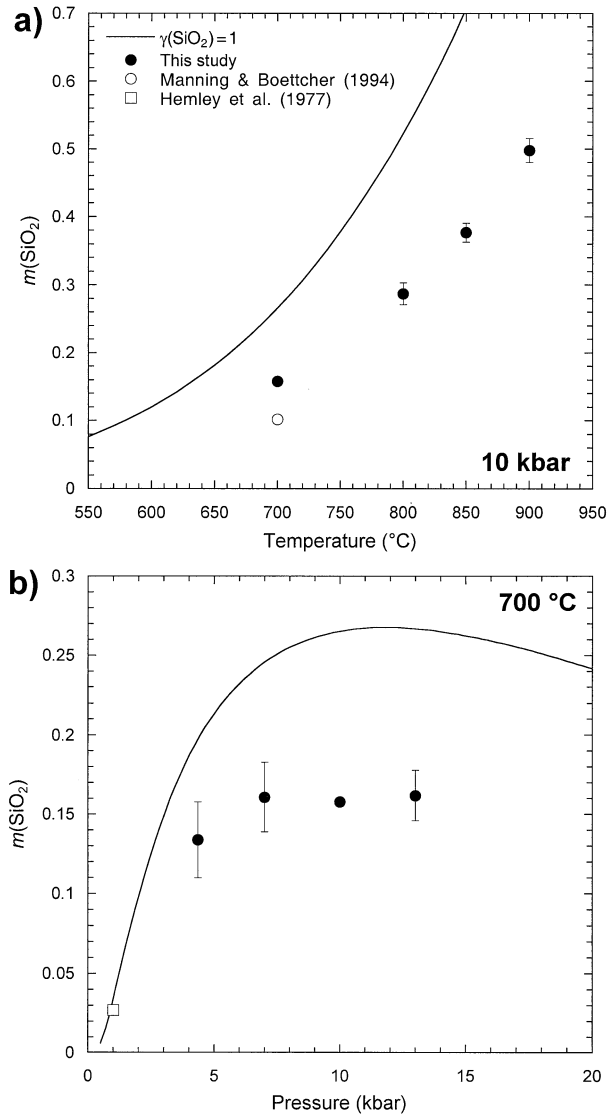

Fig. 6. Silica solubility in equilibrium with forsterite + enstatite vs. temperature at 10 kbar (A) and pressure at 700°C (B). The solid curve assumes that only silica monomers are present, and was calculated using equation of Manning (1994), together with the thermodynamic properties for enstatite, forsterite and quartz of Holland and Powell (1998). At $p > 1$ kbar, measured solubilities are lower than predicted when only monomers are assumed to be present, requiring that the activity coefficient for aqueous silica departs from unity.

ciently dilute that a_{H_2O} may be taken as unity over the present experimental PT range. The activity of $SiO_{2,aq}$ under the adopted standard state is simply the mole fraction of monomers in the solution:

$$a_S = X_1 = \gamma_S X_S \tag{9}$$

where $X_S = X_1 + 2X_2$ is the mole fraction of total silica and the subscripts 1 and 2 again refer respectively to monomer and dimer species. Combining Eqn. 8 and 9 gives:

$$K_{dm} = \frac{(1 - \gamma_S)}{2\gamma_S^2 X_S} \tag{10}$$

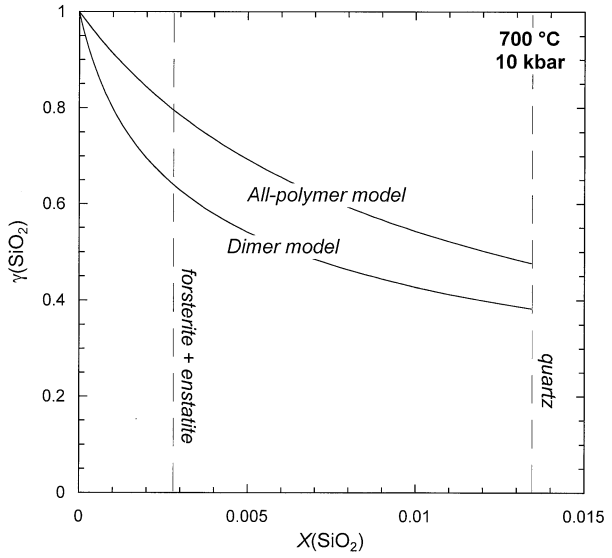

Fig. 7. Activity coefficient of aqueous silica vs. silica mole fraction at 700°C, 10 kbar, using the dimer and all-polymer models and the equilibrium constant constrained by our experiments (Table 3). Dashed vertical lines denote X_S for quartz-fluid and forsterite-enstatite-fluid equilibrium.

For a given X_s, Eqn. 10 contains two unknowns, K_{dm} and γ_S. Because K_{dm} is a constant independent of silica concentration at fixed P and T, two experiments at the same conditions but different compositions uniquely define γ_S in each experiment. Thus, for quartz and forsterite-enstatite,

$$\frac{(1 - \gamma_S^Q)}{2(\gamma_S^Q)^2 X_S^Q} = \frac{(1 - \gamma_S^{FE})}{2(\gamma_S^{FE})^2 X_S^{FE}} \tag{11}$$

Solving for γ_S^{FE} yields

$$\gamma_S^{FE} = \frac{\left(R_\gamma^2 - \frac{X_S^Q}{X_S^{FE}}\right)}{\left(R_\gamma - \frac{X_S^Q}{X_S^{FE}}\right)} \tag{12}$$

which permits calculation of K_{dm} and γ_S^Q from Eqn. 10.

Table 3 gives values of γ_S^{FE}, γ_S^Q, and $\log K_{dm}$ derived from our experiments. Calculated activity coefficients of aqueous silica assuming polymerization limited to dimers only are 0.37 to 0.72 in solutions in equilibrium with enstatite and forsterite at the experimental conditions of this study. Substantially lower values of γ_S (0.20 to 0.45) are predicted at quartz saturation. Knowledge of K_{dm} allows evaluation of the variation of γ_S with silica composition at fixed P and T. Figure 7 shows that our determination of K_{dm} at 700°C, 10 kbar (Table 3) leads to a strong decrease in γ_S at low silica concentrations with the dimer model. The compositional dependence diminishes with increasing X_S.

Values of $\log K_{dm}$ in Table 3 are ~2, consistent with ~40% polymerization of aqueous silica in equilibrium with forsterite and enstatite. Figure 8 compares $\log K_{dm}$ values derived from our 10 kbar data (Table 3), with values inferred from Raman spectroscopy at the same T and similar P (10.6 to 14 kbar; Zotov and Keppler, 2002). Although small uncertain-

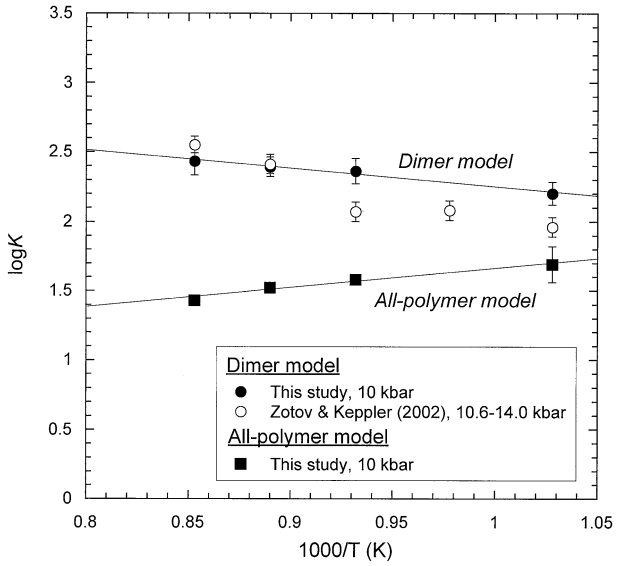

Fig. 8. Comparison of the temperature dependence of log$K$, as calculated for the dimer and all-polymer models. Values of log$K$ derived by Zotov and Keppler (2002) assuming only dimers agree well with results of this study. However, log$K$ values calculated for our results assuming an all-polymer model are lower, and yield a slope of opposite sign. Log$K$ can not be uniquely constrained unless the amounts of all polymer types can be determined precisely.

ties in the isochores in hydrothermal diamond anvil cell translate to large P uncertainty ($\sim \pm 2.5$ kbar), the insensitivity to P at these conditions make the data sets comparable. The agreement between the results of the two very different kinds of measurements is excellent.

The relationship expressed by Eqn. 10 is built on the assumption that the only solute polymers are dimers. Zotov and Keppler (2002) state that they cannot exclude the possibility that significant amounts of trimers and higher polymers are present in the form of rings or chains. Such structures could form via reactions such as:

$$\underset{\text{monomer}}{H_4SiO_4} + \underset{\text{dimer}}{H_6Si_2O_7} = \underset{\text{trimer}}{H_8Si_3O_{10}} + H_2O \qquad (13)$$

To illustrate the effect of successive attachments of SiO_4^{4-} groups to dimers, once formed, we use a simple model inspired by the molten-silicate-polymerization model of Masson (1965), where successive attachments are attended by the same K as for dimer formation; that is, the free energy of SiO_4^{4-} group attachments is independent of polymer size or shape. As shown in the Appendix, this simple "all-polymer" model leads to equilibrium constant (K_{ap}) that differs from K_{dm}:

$$K_{ap} = \frac{(1 - \gamma_S^{1/2})}{\gamma_S X_S} \qquad (14)$$

Our experimental data constrain K_{ap}, γ_S^{FE} and γ_S^{Q} derived from the all-polymer model at discrete PT conditions (Table 3). The γ_S versus X_S function at 700°C and 10 kbar is shown in Figure 7. The principal effect of postdimer polymerization is to moderate the extremely steep initial decrease of γ_S and to give higher γ_S at a given X_S.

Figure 8 illustrates that reconstructions of solute-silica speciation based on currently available data are not unique. Values of K_{ap} calculated from our experiments are lower than K_{dm} at the same P and T. Moreover, K_{ap} decreases slightly with increasing temperature. As noted by Zotov and Keppler (2002), the slope of the upper curve in Figure 8 indicates that the standard enthalpy change of reaction (7) is strongly endothermic; however, the different signs and magnitudes of the lines in Figure 8 demonstrates that the standard enthalpy change of polymerization in real SiO_2-H_2O solutions depends on the polymerization model chosen. On the other hand, it is possible that the monomeric solute silica molecule is not represented completely by H_4SiO_4, but may have additional more loosely bound, or solvated, H_2O molecules (e.g., Walther and Orville, 1983). Inclusion of solvation effects could conceivably make K greater at a given T and P than portrayed by the dimer model, regardless of polymer distribution.

4.4. Non-ideality and Critical Behavior in the System SiO_2-H_2O

To model silica solubility at very high concentrations, at temperatures and pressures approaching the second critical end point, a more explicit role of H_2O must be formulated, one in which decrease of H_2O activity must be considered. According to Zotov and Keppler (2000), each silica linkage step is a dehydration reaction, and so the H_2O/SiO_2 ratio of the polymerized species must approach unity as the polymer number increases. It may be significant in this regard that the fluid composition at the second critical end point is close to 50 mol percent SiO_2 (Kennedy et al., 1962). At this silica concentration, the fluid may be almost completely polymerized, perhaps in the form of very long chains, or more probably, as a three-dimensionally polymerized hydrous melt. In any case, the silica activity relative to the monomeric standard state would be very small. More accurate quartz solubility measurements at temperatures in the range 900 to 1050°C would be necessary to attempt to model silica-rich binary fluids by methods analogous to those useful for more dilute solutions.

4.5. Effect of Polymerization on Mineral Solubility and Silica Metasomatism

Silica activities in solutions as dilute as 0.1 mol % are significantly less than their concentrations, and this will have a major effect on calculated phase-equilibrium diagrams. Because the thermodynamic properties of aqueous silica have previously been evaluated by assuming monomeric SiO_2 at quartz saturation (e.g., Walther and Helgeson, 1977), they implicitly include the effects of polymerization but become progressively less accurate with increasing deviation from the silica concentration dictated by quartz saturation at any pressure and temperature.

The effects of polymerization on mineral solubility are illustrated in the system MgO-SiO_2-H_2O (MSH) in Figure 9, which compares aqueous silica concentrations buffered by MSH assemblages as a function of temperature at 10 kbar (Fig. 9a) and pressure at 700°C (Fig. 9b). All mineral pairs are isothermally or isobarically univariant in the presence of a SiO_2-H_2O fluid, fixing Si concentration when pressure or temperature are fixed.

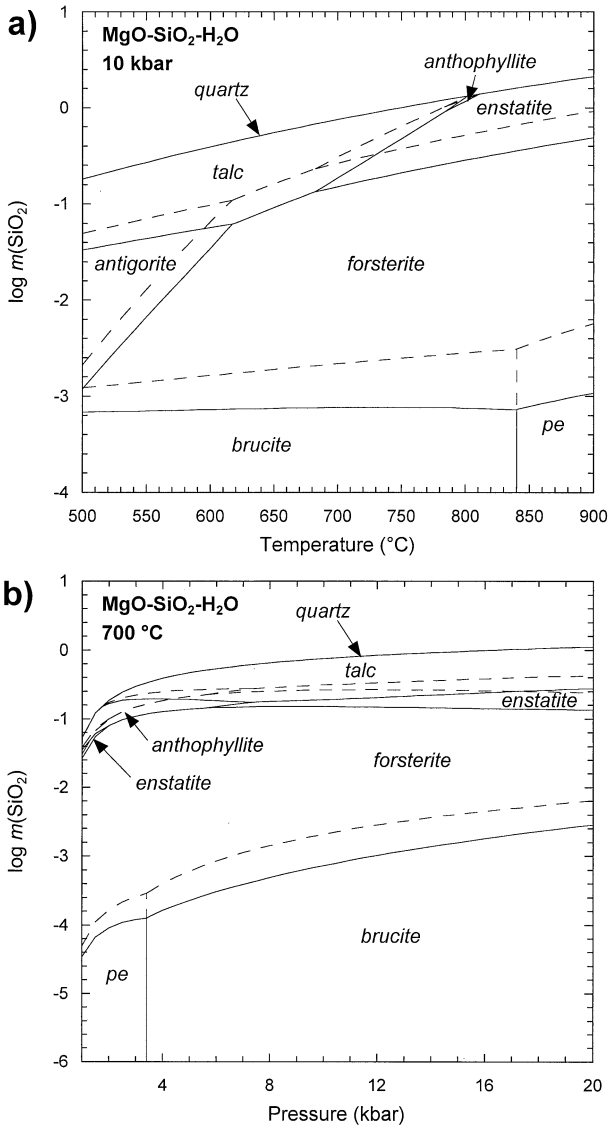

Fig. 9. Calculated phase relations in the system $MgO\text{-}SiO_2\text{-}H_2O$ in terms of silica concentration (log molality) as a function of temperature at 10 kbar (A) and as a function of pressure at 700°C (B). Solid lines show phase boundaries determined using the activity-composition model for aqueous silica; dashed lines are phase boundaries calculated assuming that only monomers are present in quartz-saturated fluids. The latter curves thus correspond to phase boundaries that would be calculated by making the conventional assumption that $\Delta G^{\circ}_{SiO_2}$ computed from quartz solubility experiments requires no activity coefficient. Abbreviation: pe, periclase.

Curves were calculated using the dimer model, with K_{dm} derived from Eqns. 6, 9 and 10 and thermodynamic properties of the MSH minerals from Holland and Powell (1998). The predicted solubilities of MSH mineral pairs are less by factors of two to three than if polymerization is ignored by calculating $\Delta G^{\circ}_{SiO_{2,aq}}$ from quartz solubility and assuming unit activity coefficient. Standard thermodynamic datasets that assume solute silica ideality cannot give accurate predictions of mineral solubilities at pressures of more than a few kilobars even at temperatures as low as 500°C.

The lower solubilities of MSH mineral pairs that result from our activity-composition relations for aqueous silica result in greater chemical-potential gradients induced by contrasts in bulk composition in geologic environments than previously believed. Silica mass transfer between quartz-saturated and quartz-undersaturated lithologies will thus be greater than that computed assuming $\gamma_S = 1$ by two to three times at all deep-crustal and mantle conditions as a consequence of the compositional dependence of silica activity.

Acknowledgments—This work was supported by NSF EAR-9909583. We thank Andy Davis for providing the synthetic enstatite and forsterite crystals grown by J. Ito. Joe Greenwood supplied the forsterite grown by H. Takei. Wayne Dollase generously assisted in the X-ray diffraction work. Natalie Caciagli helped with SEM imaging. Insightful comments by John Ferry improved an early version of the manuscript. We are especially grateful to reviewers T. Fujii, Hans Keppler and Nikolay Zotov, as well as Associate Editor Bjorn Mysen, for critical and very constructive reviews of the first-submitted version of this paper. Their reviews have greatly changed the nature of the paper. Hans Keppler kindly sent us an advance copy of the Zotov and Keppler (2002) paper while still in press.

Associate editor: B. Mysen

REFERENCES

Ague J. J. (1994) Mass transfer during Barrovian metamorphism of pelites, south-central Connecticut. I: Evidence for changes in composition and volume. *Am. J. Sci.* **294,** 989–1057.

Anderson G. M. and Burnham C. W. (1965) The solubility of quartz in supercritical water. *Am. J. Sci.* **263,** 494–511.

Aranovich L. Y. and Newton R. C. (1998) Reversed determination of the reaction: phlogopite + quartz = enstatite + potassium feldspar + H_2O in the ranges 750–875°C and 2–12 kbar at low H_2O activity with concentrated KCl solutions. *Am. Min.* **183,** 193–204.

Bebout G. E. and Barton M. D. (1989) Fluid flow and metasomatism in a subduction zone hydrothermal system: Catalina Schist terrane, California. *Geology* **17,** 976–980.

Bell D. R. and Rossman G. R. (1992) Water in Earth's mantle: The role of nominally anhydrous minerals. *Science* **255 ,** 1391–1397.

Berman R. G. (1988) Internally consistent thermodynamic data for minerals in the system $Na_2O\text{-}K_2O\text{-}CaO\text{-}MgO\text{-}FeO\text{-}Fe_2O_3\text{-}Al_2O_3\text{-}SiO_2\text{-}TiO_2\text{-}H_2O\text{-}CO_2$. *J. Petrol.* **29,** 445–522.

Ferry J. M. (1994) A historical review of metamorphic fluid flow. *J. Geophys. Res.* **99,** 15,487–15,498.

Fourier R. O. and Potter R. W. II (1982) An equation correlating the solubility of quartz in water from 25° to 900°C at pressures up to 10,000 bars. *Geochim. Cosmochim. Acta* **46,** 1969–1973.

Hemley J. J., Montoya J. W., Shaw D. R., and Luce R. W. (1977) Mineral equilibria in the $MgO\text{-}SiO_2\text{-}H_2O$ system: II. Talc-antigorite-anthophyllite-enstatite stability relations and some geological implications in the system. *Am. J. Sci.* **277,** 322–351.

Holland T. J. B. and Powell R. (1998) An internally consistent thermodynamic data set for phases of petrologic interest. *J. Metamorph. Geol.* **16,** 309–343.

Ito J. (1975) High temperature solvent growth of orthoenstatite, $MgSiO_3$, in air. *Geophys. Res. Lett.* **2,** 533–536.

Kennedy G. C., Wasserburg G. J., Heard H. C., and Newton R. C. (1962) The upper three-phase region in the system $SiO_2\text{-}H_2O$. *Am. J. Sci.* **260,** 501–521.

Manning C. E. (1994) The solubility of quartz in the lower crust and upper mantle. *Geochim. Cosmochim. Acta* **58,** 4831–4839.

Manning C. E. (1995) Phase-equilibrium controls on SiO_2 metasomatism by aqueous fluids in subduction zones: Reaction at constant pressure and temperature. *Int. Geol. Rev.* **37,** 1074–1093.

Manning C. E. and Boettcher S. L. (1994) Rapid-quench hydrothermal experiments at mantle pressures and temperatures. *Am. Min.* **79,** 1153–1158.

Masson C. R. (1965) An approach to the problem of ionic distribution in liquid silicates. *Proc. Royal Soc. London* **A287,** 201–221.

Nakamura Y. and Kushiro I. (1974) Composition of the gas phase in Mg_2SiO_2-SiO_2-H_2O at 15 kbar. *Carn. Inst. Wash. Year Book* **73,** 255–258.

Newton R. C. and Manning C. E. (2000a) Metasomatic phase relations in the system CaO-MgO-SiO_2-H_2O-NaCl at high temperatures and pressures. *Int. Geol. Rev.* **42,** 152–162.

Newton R. C. and Manning C. E. (2000b) Quartz solubility in concentrated aqueous NaCl solutions at deep crust-upper mantle metamorphic conditions: 2–15 kbar and 500–900°C. *Geochim. Cosmochim. Acta* **64,** 2993–3005.

Schreyer W. and Yoder H. S. Jr. (1964) The system Mg-Cordierite-H_2O and related rocks. *Neues Jarbuchfür Mineralogie, Abhandlungen* **101,** 271–342.

Takei H. and Hosoya S. (1985) Growth of $MnSiO_3$ and (Mn,Mg)SiO_3 crystals by the floating zone method. *J. Crystal Growth* **71,** 17–22.

Walther J. V. and Helgeson H. C. (1977) Calculation of the thermodynamic properties of aqueous silica and the solubility of quartz and its polymorphs at high pressures and temperatures. *Am. J. Sci.* **277,** 1315–1351.

Walther J. V. and Orville P. M. (1983) The extraction-quench technique for determination of the thermodynamic properties of solute complexes: Application to quartz solubility in fluid mixtures. *Am. Min.* **68,** 731–741.

Zhang Y.-G. and Frantz J. D. (2000) Enstatite-forsterite-water equilibria at elevated temperatures and pressures. *Am. Min.* **85,** 918–925.

Zotov N. and Keppler H. (2000) In-situ Raman spectra of dissolved silica species in aqueous fluids to 900°C and 14 kbar. *Am. Min.* **85,** 600–603.

Zotov N. and Keppler H. (2002) Silica speciation in aqueous fluids at high pressures and high temperatures. *Chem. Geol.* **184,** 71–82.

APPENDIX

It is possible that significant amounts of trimers, quadrimers and higher polymers are formed by successive attachment to dimers, once formed. The simplest assumption to characterize the concentrations of polymeric groups is to regard K as independent of polymer size (Masson, 1965). This is equivalent to the assumption that the Gibbs free energy of an attachment reaction is governed mainly by the local electrostatic environment of the attachment site (an SiO_4^{4-} group) and less on the influence of neighboring groups. The assumption of size-independent K will be more nearly valid when the attachment occurs at the ends of long chains. The polymerized species are assumed to be hydrous molecules, and each polymerization step is a dehydration reaction as per Eqn. 7 and 13, text. The activity of H_2O is sensibly unity over the dilute concentration range considered here. From the mass-action expression for polymerization-step reactions, the equilibrium constant for the "all-polymer" model, K_{ap}, is

$$K_{ap} = \frac{X_n}{X_{n-1}X_1} \tag{A1}$$

where n is polymer number. Combination with Eqn. 8, text, gives

$$X_n = X_1^n K_{ap}^{n-1} \tag{A2}$$

Mass balance requires that

$$X_S = X_1 + 2X_2 + 3X_3 + \ldots + nX_n \tag{A3}$$

which can be combined with Eqn. A2 to give

$$K_{ap}X_S = \sum_{n=0}^{\infty} n(K_{ap}X_1)^n \tag{A4}$$

The infinite series converges to $K_{ap}X_1/(1 - K_{ap}X_1)^2$ provided that $K_{ap}X_1 < 1$, which is always true because $X_S > X_1$. Therefore

$$X_S = \frac{X_1}{(1 - K_{ap}X_1)^2} \tag{A5}$$

which can be combined with Eqn. 9, text, to give

$$K_{ap} = \frac{1 - \gamma_S^{1/2}}{\gamma_S X_S} \tag{A6}$$

Equation A6 is the all-polymer analog of Eqn. 10, text, in which K_{ap} is independent of polymer size. By the arguments used to derive Eqn. 12, text, γ_S^{FE} is

$$\gamma_S^{FE} = \left(\frac{R_\gamma^{1/2} - X_S^{Qz}/R_\gamma^{1/2}X_S^{FE}}{1 - X_S^{Qz}/R_\gamma^{1/2}X_S^{FE}} \right)^2 \tag{A7}$$

which allows calculation of K_{ap} and γ_S^Q by back substitution into Eqn. A6.